Proceedings of the 11th International Conference on Fluid Flow, Heat and Mass Transfer (FFHMT 2024)
Chestnut Conference Centre - University of Toronto, Toronto, Canada – June 16-18, 2024
Paper No. 116
DOI: 10.11159/ffhmt24.116

Convective Heat Transfer in a Porous Medium under LTNE: Impacts of Heterogeneous Permeability and Sinusoidal Wall Temperature

Mohammad M. Rahman
Department of Mathematics, College of Science, Sultan Qaboos University
PO Box 36, PC 123 Al-Khod, Muscat, Oman
mansur@squ.edu.om

Abstract – This paper investigates numerically and statistically the impacts of sinusoidal wall temperature variation on the free convective temporal heat transfer flow inside a rectangular enclosure filled with glass bead porous medium under the local thermal non-equilibrium conditions for the working fluid and the porous medium. The fluid's thermal conductivity is considered variable, and a Darcy-Brinkman-Forchheimer model is applied to model the fluid flow. The constitutive equations that govern the flow and heat transfer are simulated using the Galerkin-type finite element method. The CFD (computational fluid dynamics) and RSM (response surface methodology) results revealed that glass bead diameter, porosity, frequency, and wave amplitude significantly impact the heat transfer rate and friction factor.

***Keywords*:** Convection, heat transfer, porous media, non-Darcy model, local thermal non-equilibrium, permeability

1. Introduction

Porous media are used in various industrial and natural processes, including geothermal system management, hydrocarbon reservoirs, absorption and adsorption processes, heat pipes, packed filters, phase change applications, toxin dispersal in groundwater, micro heat exchangers, and transpiration cooling [1-4]. Additionally, porous layers and insertions as heat sink mediums show promise in developing sophisticated new technologies. The importance of convective heat transmission in porous media has increased significantly over the years. Al-Weheibi et al. [5] studied three-dimensional convective heat transfer flow in a right trapezoidal cavity, considering local thermal non-equilibrium (LTNE) between the working fluid and the glass bead permeable matrix. They identified the role of the medium's porosity and permeability on the LTNE to LTE states and vice versa. Furthermore, the investigation by Al Hajri et al. [6] confirmed that the Darcy and Brinkman numbers and the interphase heat transfer coefficient strongly influence LTNE. The numerical investigation by Astanina and Sheremet [7] determined whether varying the viscosity of the working liquid could effectively control fluid flow and heat transmission under LTNE.

The study conducted by Varol et al. [8] on sinusoidally varying temperatures in a porous region revealed that the strength of heat transfer increases as the amplitude of thermal oscillation increases. Sheremet and Oztop [9] conducted a study on thermo-gravitational convection under LTE inside a square geometry with sinusoidally heated wall conditions and found that the insertion and position of the porous block significantly amplifies heat transmission. When studying the flow and heat transfer characteristics in a porous medium, it is essential to consider permeability variation, which has yet to be overlooked in the literature, with only a few works discussing it [10-11]. Recently, Rahman et al. [12] explored the transient non-Darcy flow and heat transfer in a heterogeneous porous medium inside a square porous cavity under LTNE and sinusoidally varying thermal boundary conditions. Their results needed more statistical analysis to determine the optimum heat transfer rate. Our research thus aims to fill the gap in the existing literature incorporating the RSM by exploring the combined impacts of heterogeneous permeability and sinusoidal temperature variation on the convective transient flow inside a porous reservoir under LTNE following the non-Darcy approach of Rahman et al. [12].

2. Physical Model Description

Let us consider the unsteady two-dimensional free convection flow of a viscous incompressible fluid inside a rectangular cavity of height H and width W filled with glass bead porous medium. The geometric configuration is

depicted in Fig. 1. The $x-$ axis is taken along the lower wall of the cavity whereas the $y-$ is taken along the near wall of it. The origin is located at the lower left corner of the cavity. The gravity acts downwards along the $y-$ direction. The left wall of the cavity is hot (T_h) whose temperature varies sinusoidally as $T = T_c + \Delta T\left(B^* / H\right)\sin\left(n\pi y / H\right)$ whereas the right vertical wall is cold ($T_c < T_h$), where $\Delta T = T_h - T_c$, B^* is the wave amplitude, and n is the frequency of the wave. The cavity has adiabatic bottom and top walls, which means that heat cannot escape in the direction perpendicular to the walls.

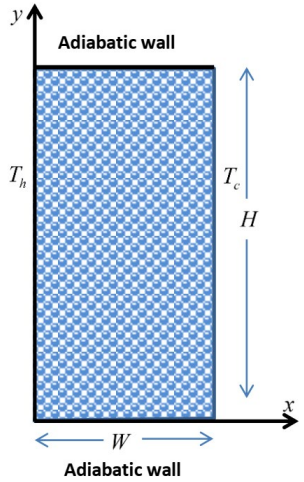

Fig. 1: Flow configuration and coordinate system.

The working fluid (water) and the porous matrix have different temperatures T_f and T_s respectively, and therefore, two energy equations are considered to account for the heat transmission. The Darcy-Brinkman-Forchheimer model is used to describe fluid flow in a porous medium due to the high permeability of the medium. The fluid does not slip on the solid walls. To consider the density variation in the buoyancy force, the Oberbeek-Boussinesq approximation is applied.

Following [4], [10-11] and Rahman et al. [12] the dimensionless governing equations for the above-described model are as follows:

$$U_X + V_Y = 0 \tag{1}$$

$$U_\tau = -P_X - (\varepsilon_p Dp / Da\,\mathrm{Re}_p)U + (Dp/\mathrm{Re}_p)\nabla^2 U - (\varepsilon_p C_F / \sqrt{Da})U\sqrt{U^2+V^2} \tag{2}$$

$$V_\tau = -P_Y - (\varepsilon_p Dp / Da\,\mathrm{Re}_p)V + (Dp/\mathrm{Re}_p)\nabla^2 V - (\varepsilon_p C_F / \sqrt{Da})V\sqrt{U^2+V^2} + \varepsilon_p\theta_f \tag{3}$$

$$\begin{aligned}\varepsilon_p(\theta_f)_\tau + U(\theta_f)_X + V(\theta_f)_Y = (Dp/\mathrm{Pr}\,\mathrm{Re}_p)\left[\left(\kappa_X(\theta_f)_X\right)_X + \left(\kappa_Y(\theta_f)_Y\right)_Y\right] \\ +[6(1-\varepsilon_p)/(\mathrm{Pr}\,\mathrm{Re}_p\,Dp)][2+1.1\mathrm{Pr}^{1/3}\,\mathrm{Re}_p^{0.6}](\theta_s-\theta_f)\end{aligned} \tag{4}$$

$$(\theta_s)_\tau = (\xi Dp/\mathrm{Pr}\,\mathrm{Re}_p)\left[\nabla^2\theta_s\right] - [6\xi/(\gamma\,\mathrm{Pr}\,\mathrm{Re}_p\,Dp)][2+1.1\mathrm{Pr}^{1/3}\,\mathrm{Re}_p^{0.6}](\theta_s-\theta_f) \tag{5}$$

The initial ($\tau = 0$) and boundary ($\tau > 0$) conditions are

For $\tau = 0$: $\mathbf{V} = \mathbf{0}$ and $\theta_f = \theta_s = \theta_{in}$ (6)

For $\tau > 0$: $\mathbf{V} = \mathbf{0}$, $\theta_f = B0\sin\left(n\pi Y\right)$, $\theta_s = B0\sin\left(n\pi Y\right)$ for $X = 0$ and $0 \le Y \le 1$ (7)

$$\mathbf{V} = \mathbf{0},\ \theta_f = \theta_s = 0 \text{ for } X = Ar \text{ and } 0 \le Y \le 1 \tag{8}$$

$$\mathbf{V} = \mathbf{0},\ \left(\theta_f\right)_Y = \left(\theta_s\right)_Y = 0 \text{ for } Y = 0 \text{ and } 0 \le X \le Ar \tag{9}$$

$$\mathbf{V} = \mathbf{0},\ \left(\theta_f\right)_Y = \left(\theta_s\right)_Y = 0 \text{ for } Y = 1 \text{ and } 0 \le X \le Ar \tag{10}$$

The dimensionless parameters appeared in Eqs. (1)-(10) are pore diameter $Dp = dp / H$, Darcy number $Da = (K / H^2) = \varepsilon_p^3 Dp^2 / [150(1-\varepsilon_p)^2]$, diffusivity ratio $\xi = \alpha_s / \alpha_f$, conductivity ratio $\gamma = \kappa_s / \kappa_f$, aspect ratio $Ar = W / H$, wave amplitude $B0 = B^* / H$, X-component of conductivity ratio $\kappa_X = \left[\varepsilon_p + 0.5 \Pr \mathrm{Re}_p\right]$, Y-component of conductivity ratio $\kappa_Y = \left[\varepsilon_p + 0.1 \Pr \mathrm{Re}_p\right]$.

The nondimensional Nusselt numbers for fluid and solid are defined as

$$Nuf = -\int_0^1 \left(\varepsilon_p + 0.1 \Pr \mathrm{Re}_p\right)\left((\theta_f)_X\right)_{X=0} dY \tag{11}$$

$$Nus = -\int_0^1 \left(\varepsilon_p + 0.1 \Pr \mathrm{Re}_p\right)\left((\theta_s)_X\right)_{X=0} dY \tag{12}$$

The skin friction coefficient or nondimensional shear rate is defined by

$$Cf = (2Dp / \mathrm{Re}_p)\left(V_X\right)_{X=0} \tag{13}$$

3. Method of Solution

The complex model equations (1)-(5) possess no analytical solution; we solve them using finite element-based software COMSOL Multiphysics (see Uddin and Rahman [13]). The simulated results are validated with De Vahl Davis [14] as tabulated in Table 1. The validation data echoed nicely among them.

Table 1: Code validation through average Nusselt number (Nuf) for different values of the Rayleigh number.

Nuf	$Ra = 10^3$	$Ra = 10^5$	$Ra = 10^6$
Present	1.1178	4.5216	8.8278
De Vahl Davis [14]	1.118	4.519	8.800
|Error| = [14]-present	1.79×10^{-4}	5.75×10^{-4}	3.13×10^{-3}

3. Results and Discussion

For numerical simulation, we used water as the working fluid and glass ball as the permeable matrix to explore the impacts of the sinusoidal wall temperature and heterogeneous permeability on the thermal and flow fields. The model parameter ranges are: $0.01 \le Dp \le 0.19$, $0.65 \le \varepsilon_p \le 0.95$, $1 \le n \le 3$, $0.1 \le B0 \le 1.1$ keeping $\mathrm{Re}_p = 100$, $\Pr = 6.84$, and $Ar = 0.5$ fixed.

3.1. Impacts of the Wave Amplitude

Figure 2 shows that the amplitude of the wave affects the structure of the streamlines (1st column), fluid (2nd column), and solid matrix (3rd column) isotherms. Smaller wave amplitudes create two vertically elongated counter-clockwise rotating vortices, while larger amplitudes make them circular and move them to the top and bottom of the cavity. The left wall of the upper vortex has the highest velocity magnitude. Higher amplitudes result in a more robust fluid flow. For smaller wave amplitudes, isotherms for the fluid (2nd column) show complex vortices and higher temperatures at the

lower mid-plane of the cavity. At higher wave amplitudes, isotherms turn into parabolic shapes, with the bottom region containing more heat. For the solid matrix, the isotherms (3rd column) form thermal boundary layers on both sides of the left hot and right cold walls at smaller wave amplitudes. The isotherms evolve from the left wall and move towards the cold right wall for larger wave amplitudes.

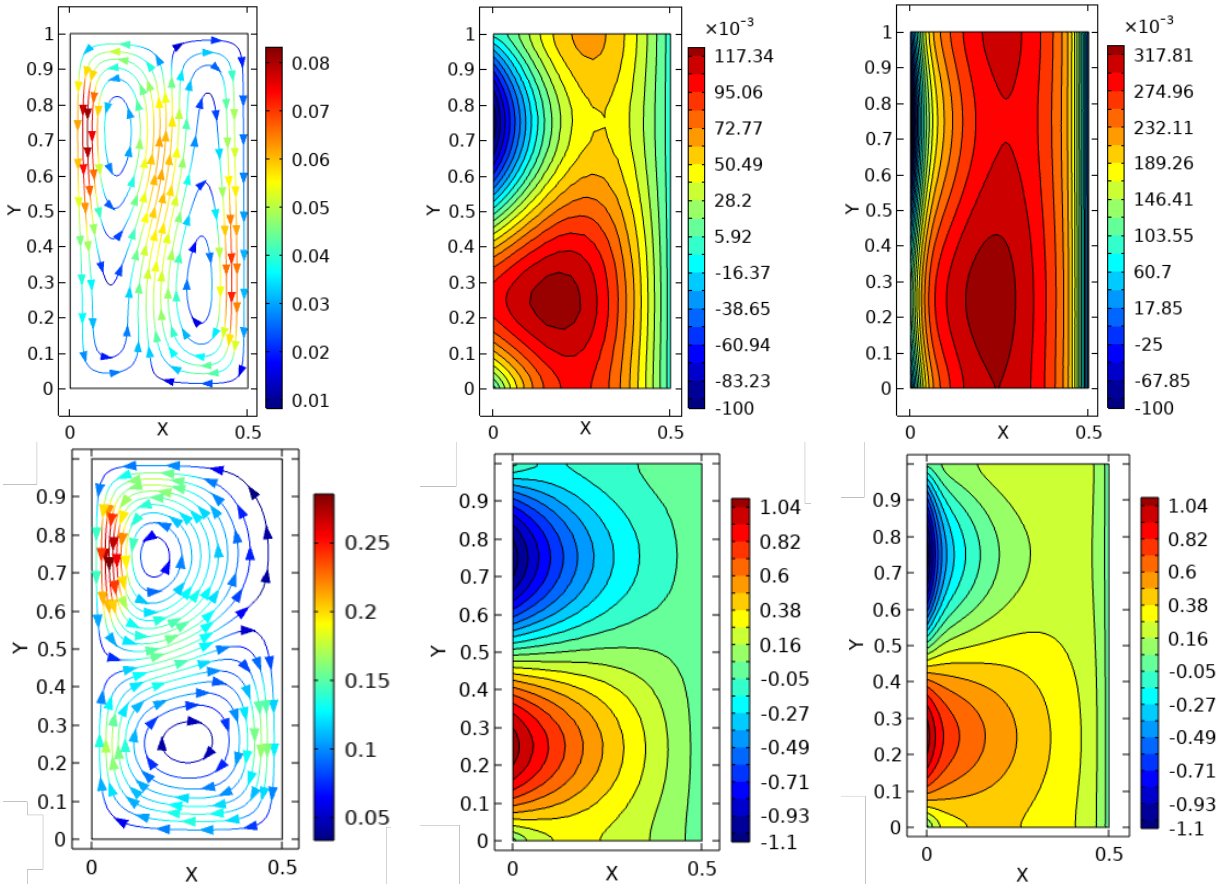

Fig. 2: Streamlines (1st column), isolines of (θ_f) (2nd column), and isolines of (θ_s) (3rd column) for different values of $B0 = 0.1$ (1st row), and $B0 = 1.1$ (2nd row) when $\mathrm{Re}_p = 100$, $\mathrm{Pr} = 6.84$, $n = 2$, $\varepsilon_p = 0.95$ at time $\tau = 1$.

The fluid temperature oscillates at a high frequency, affecting the pressure. In some parts of the enclosure, the fluid temperature becomes colder than the ambient temperature. In Figure 3, we see how the wave frequency ($n = 1$ and $n = 2$) affects the streamlines and isotherms. When $n = 1$, an anticlockwise rotating vortex covers the entire plane, with the maximum velocity near the right wall. When $n = 2$, two rotating vortices appear, leading to a complex structure of the streamlines. The second column shows the temperature distribution for two frequencies, $n = 1$ and $n = 2$. For $n = 1$, there is strong convection in the middle of the hot left wall, while for $n = 2$, there are alternating hot and cold regions on the hot wall. The isolines elongate towards the right wall of the cavity. A thermal boundary layer forms on the cold wall and becomes thinner with higher wave frequency. Higher n reduces the temperature difference between the hot and cold walls.

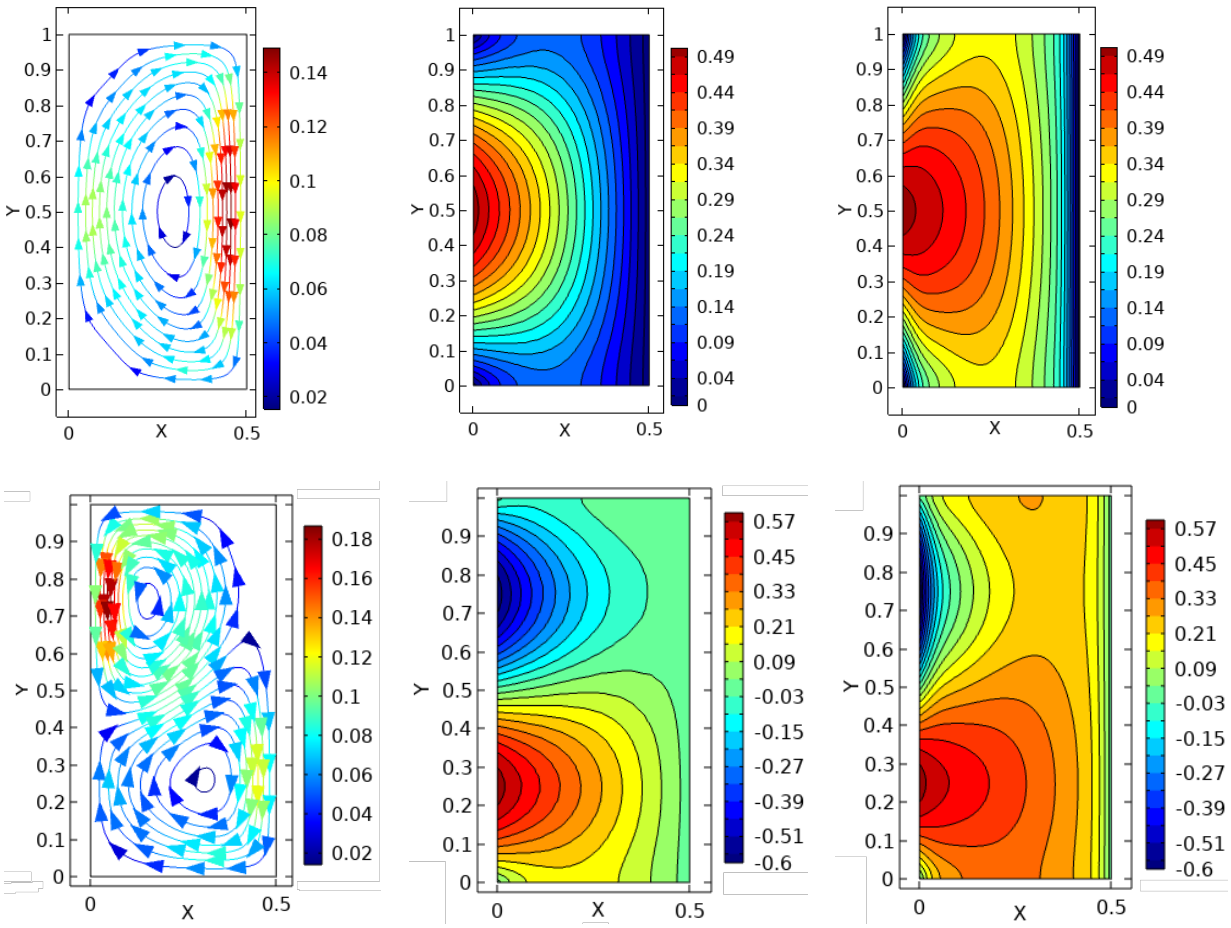

Fig. 3: Streamlines (1st column), isolines of (θ_f) (2nd column), and isolines of (θ_s) (3rd column) for different values of $n=1$ (1st row), and $n=2$ (2nd row) when $\mathrm{Re}_p=100$, $\mathrm{Pr}=6.84$, $B0=0.6$, $\varepsilon_p=0.95$ at time $\tau=1$.

3.2. Statistical Data Analysis

The response surface (RS) approach is used to optimize and model the relationship between a response (RP) variable and multiple input variables (see [15-17]). The response surface methodology (RSM) involves seven steps, including selecting the response, assigning codes to the variables, developing a trial scheme for response, performing regression analysis, forming a quadratic polynomial, creating a 2D contour strategy or 3D surface, and analyzing the optimal operating settings. The RSM is adopted to verify the accuracy of CFD results. The second-order RSM considers all linear, square, and collaboration mechanisms for guessing the response when the effect of target parameters (Dp, ep, $B0$, and n) on the response functions (Nuf, Nus, and Cf) for the studied model is taken into account.

Consider the regression setup as follows (see, [Huda et al. [17])

$$y=a_0+\sum_{i=1}^{4}a_i x_i+\sum_{i=1}^{4}a_{ii}x_i^2+\sum_{i=1}^{4}\sum_{j=1}^{4}a_{ij}x_i x_j\,|_{i<j}+r \tag{14}$$

Here, y represents the response functions Nuf, Nus, and Cf, and x_i and x_j stands for the input variables Dp, ep, $B0$, and n. The a_i's are the constant coefficients and r is the error. The target is to establish an excellent fit between the response variables and response functions. Box and Wilson [15] proposed the central composite (CC) scheme

to fit the second-order RSM model. See Table 2 for the coded levels and design parameters. Eqn. (14) can be substituted with input parameters as follows:

$$y = a_0 + a_1 Dp + a_2 ep + a_3 B0 + a_4 n + a_{11} Dp^2 + a_{22} ep^2 + a_{33} B0^2 + a_{44} n^2 + a_{12} Dpep + a_{13} DpB0 + a_{14} Dpn + a_{23} epB0 + a_{24} epn + a_{34} B0n \quad (15)$$

To establish an accurate relationship between input variables (Dp, ep, $B0$, and n) and the resulting response functions (Nuf, Nus, and Cf), coefficients in (15) must first be determined. Simulation results were presented in Table 3 for suggested and actual values generated through the central composite design. Statistical analysis of the standard model using the RSM is shown in Tables 4-7 with the ANOVA scheme. The F-value indicates the data's variability around the mean, while the p-value determines the likelihood of the null hypothesis. The R^2 value measures how much variability in the observed response value can be explained by the experimental factors. Each term of Eq. (15) has its own statistical indicators when the distinct parameters are selected. With an R^2 value of 99.71% (Table 4) for Nuf, Dp, n, Dp^2, $DpB0$, and $B0n$ are important model expressions. The classical F-value of 362.71 suggests the model is significant, with a p-value of less than 5%. Thus, the final regression model equation for Nuf (Table 7) becomes

$$Nuf = 203.23 - 2628.13 Dp - 127.08 B0 + 25.33 n + 8818.72 Dp^2 + 684.12 DpB0 + 163.94 B0n \quad (16)$$

Similarly, the regression model equations for Nus and Cf become

$$Nus = 333.86 + 1097.55976 Dp - 698.04 B0 + 541.73 n + 436.33 B0^2 - 137.50 n^2 + 212.29 B0n \quad (17)$$

$$Cf = -0.002902 - 0.027723\, Dp + 0.003975 ep - 0.011045\, B0 + 0.066624 DpB0 + 0.016988 epB0 \quad (18)$$

Table 2: Designed factors (variables) and coded levels for composite central design (CCD).

Actual Factors (variables) Name	Coded Factors (variables) Name	Level		
		-1 (low)	0 (medium)	1 (high)
Dp	A	0.01	0.1	0.19
ep	B	0.65	0.8	0.95
$B0$	C	0.1	0.6	1.1
n	D	1	2	3

Table 3: Levels for input factors and output (response) functions.

Run order	Coded values					Actual values					Observed Response functions		
	A	B	C	D		Dp	ep	$B0$	n		Nuf	Nus	Cf
1	0	0	0	0		0.1	0.8	0.6	2		206.99	473.86	0.0055585
2	1	-1	-1	-1		0.19	0.65	0.1	1		16.592	310.07	0.00054035
3	0	0	0	0		0.1	0.8	0.6	2		206.99	473.86	0.0055585
4	1	1	1	1		0.19	0.95	1.1	3		538.9	827.34	0.015266
5	1	0	0	0		0.19	0.8	0.6	2		201.73	460.45	0.0074778
6	1	1	-1	1		0.19	0.95	0.1	3		48.6	332.56	0.0022873
7	1	-1	1	1		0.19	0.65	1.1	3		537.31	839.98	0.0063341
8	-1	-1	0	1		0.01	0.65	0.1	3		245.58	288.25	0.00037477
9	0	0	0	1		0.1	0.8	0.6	3		293.62	475.99	0.0042932
10	-1	0	0	0		0.01	0.8	0.6	2		353.91	402.09	0.0015136
11	-1	1	-1	1		0.01	0.95	0.1	3		264.5	301.8	0.0044809
12	0	1	0	0		0.1	0.95	0.6	2		208.53	466.07	0.0091773

13	0	0	0	0		0.1	0.8	0.6	2		206.99	473.86	0.0055585
14	1	1	-1	-1		0.19	0.95	0.1	1		16.747	298.38	0.0006047
15	1	-1	-1	1		0.19	0.65	0.1	3		48.446	345.14	0.000577
16	0	0	0	0		0.1	0.8	0.6	2		206.99	473.86	0.0055585
17	1	1	1	-1		0.19	0.95	1.1	1		209	354.67	0.022301
18	-1	1	1	1		0.01	0.95	1.1	3		661.07	742.55	0.0052491
19	-1	-1	1	1		0.01	0.65	1.1	3		642.86	728.65	0.00059278
20	0	0	0	0		0.1	0.8	0.6	2		206.99	473.86	0.0055585
21	-1	1	-1	-1		0.01	0.95	0.1	1		238.12	273.15	0.0040341
22	0	0	1	0		0.1	0.8	1.1	2		377.78	765.36	0.009737
23	0	0	0	0		0.1	0.8	0.6	2		206.99	473.86	0.0055585
24	-1	-1	1	-1		0.01	0.65	1.1	1		262.26	293.86	0.00060336
25	-1	1	1	-1		0.01	0.95	1.1	1		273.61	302.47	0.0040615
26	0	0	0	-1		0.1	0.8	0.6	1		107.09	165.42	0.0048537
27	0	-1	0	0		0.1	0.65	0.6	2		205.89	484.88	0.0025657
28	0	0	-1	0		0.1	0.8	0.1	2		43.220	369.22	0.0024242
29	1	-1	1	-1		0.19	0.65	1.1	1		208.7	363.47	0.0093705
30	-1	-1	-1	-1		0.01	0.65	0.1	1		220.64	260.38	0.00032391

Table 4: Analysis of variance (ANOVA) for Nuf .

Source	DOF	SS	Adj. SS	F-Value	p-Value	Comment
Model	14	7.917E+05	56546.81	362.71	< 0.0001	significant
Dp	1	99238.84	99238.84	636.55	< 0.0001	significant
ep	1	278.47	278.47	1.79	0.2013	insignificant
B	1	3.667E+05	3.667E+05	2351.92	< 0.0001	significant
n	1	1.659E+05	1.659E+05	1064.22	< 0.0001	significant
$Dp.ep$	1	254.09	254.09	1.63	0.2211	insignificant
$Dp.B$	1	15163.77	15163.77	97.27	< 0.0001	significant
$Dp.n$	1	590.04	590.04	3.78	0.0707	insignificant
$ep.B$	1	1.73	1.73	0.0111	0.9175	insignificant
$ep.n$	1	5.75	5.75	0.0369	0.8503	insignificant
$B.n$	1	1.075E+05	1.075E+05	689.60	< 0.0001	significant
Dp^2	1	13220.07	13220.07	84.80	< 0.0001	significant
ep^2	1	1.75	1.75	0.0112	0.9170	insignificant
B^2	1	43.80	43.80	0.2810	0.6038	insignificant
n^2	1	94.31	94.31	0.6049	0.4488	insignificant
Residual	15	2338.52	155.90	-	-	
Lack of Fit	10	2338.52	233.85	-	-	
Pure Error	5	0.0000	0.0000	-	-	
Cor. Total	29	7.940E+05	-	-	-	

*Here, $R^2 = 99.71\%$, Adjusted $R^2 = 99.43\%$, Predicted $R^2 = 98.22\%$, Adeq. Precision = 71.86

Table 5: Analysis of variance (ANOVA) for Nus.

Source	DOF	SS	Adj. SS	F-Value	p-Value	Comment
Model	14	8.846E+05	63185.51	78.48	< 0.0001	significant
Dp	1	16131.67	16131.67	20.04	0.0004	significant
ep	1	13.68	13.68	0.0170	0.8980	insignificant
B	1	3.306E+05	3.306E+05	410.61	< 0.0001	significant
n	1	2.839E+05	2.839E+05	352.56	< 0.0001	significant
$Dp.ep$	1	558.61	558.61	0.6938	0.4179	insignificant
$Dp.B$	1	1508.55	1508.55	1.87	0.1912	insignificant
$Dp.n$	1	473.50	473.50	0.5881	0.4551	insignificant
$ep.B$	1	0.0600	0.0600	0.0001	0.9932	insignificant
$ep.n$	1	0.1122	0.1122	0.0001	0.9907	insignificant
$B.n$	1	1.803E+05	1.803E+05	223.89	< 0.0001	significant
Dp^2	1	1880.12	1880.12	2.34	0.1473	insignificant
ep^2	1	772.47	772.47	0.9594	0.3429	insignificant
B^2	1	30828.88	30828.88	38.29	< 0.0001	significant
n^2	1	48986.56	48986.56	60.84	< 0.0001	significant
Residual	15	12076.81	805.12	-	-	-
Lack of Fit	10	12076.81	1207.68	-	-	-
Pure Error	5	0.0000	0.0000	-	-	-
Cor. Total	29	8.967E+05	-	-	-	-

*Here, $R^2 = 98.65\%$, Adjusted $R^2 = 97.40\%$, Predicted $R^2 = 94.22\%$, Adeq. Precision = 32.10

Table 6: Analysis of variance (ANOVA) for Cf.

Source	DOF	SS	Adj. SS	F-Value	p-Value	Comment
Model	10	0.0006	0.0001	23.45	< 0.0001	significant
Dp	1	0.0001	0.0001	41.13	< 0.0001	significant
ep	1	0.0001	0.0001	46.30	< 0.0001	significant
B	1	0.0002	0.0002	72.70	< 0.0001	significant
n	1	2.910E-06	2.910E-06	1.14	0.2996	insignificant
$Dp.ep$	1	3.712E-06	3.712E-06	1.45	0.2433	insignificant
$Dp.B$	1	0.0001	0.0001	56.20	< 0.0001	significant
$Dp.n$	1	6.284E-06	6.284E-06	2.46	0.1336	insignificant
$ep.B$	1	0.0000	0.0000	10.15	0.0049	insignificant
$ep.n$	1	3.596E-08	3.596E-08	0.0141	0.9069	insignificant
$B.n$	1	7.716E-06	7.716E-06	3.02	0.0987	insignificant
Residual	19	0.0000	2.559E-06	-	-	
Lack of Fit	14	0.0000	3.473E-06	-	-	
Pure Error	5	0.0000	0.0000	-	-	
Cor. Total	29	0.0006	-	-	-	

*Here, $R^2 = 92.51\%$, Adjusted $R^2 = 88.56\%$, Predicted $R^2 = 52.65\%$, Adeq. Precision = 21.37

Table 7: Predictable regression coefficients for Nuf, Nus, and Cf from RSM.

Coefficient	*Nuf*		*Nus*		*Cf*	
	values	p-values	values	p-values	values	p-values
a_0	203.23357	-	333.85997	-	-0.002902	-
a_1	-2628.13066	< 0.0001	1097.55976	0.0004	-0.027723	< 0.0001
a_2	-8.05013	0.2013	-1190.53982	0.8980	0.003975	< 0.0001
a_3	-127.07811	< 0.0001	-698.04326	< 0.0001	-0.011045	< 0.0001
a_4	25.32576	< 0.0001	541.72739	< 0.0001	0.001380	0.2996
a_{11}	8818.72428	< 0.0001	-3325.68768	0.1473	-	-
a_{22}	36.51852	0.9170	767.41910	0.3429	-	-
a_{33}	16.44667	0.6038	436.32772	< 0.0001	-	-
a_{44}	-6.03333	0.4488	-137.50307	< 0.0001	-	-
a_{12}	-295.18981	0.2211	-437.68519	0.4179	0.035677	0.2433
a_{13}	684.11806	< 0.0001	215.77778	0.1912	0.066624	< 0.0001
a_{14}	-67.47431	0.0707	60.44444	0.4551	-0.006963	0.1336
a_{23}	-4.38250	0.9175	-0.816667	0.9932	0.016988	0.0049
a_{24}	3.99542	0.8503	0.558333	0.9907	-0.000316	0.9069
a_{34}	163.94287	< 0.0001	212.28500	< 0.0001	-0.001389	0.0987

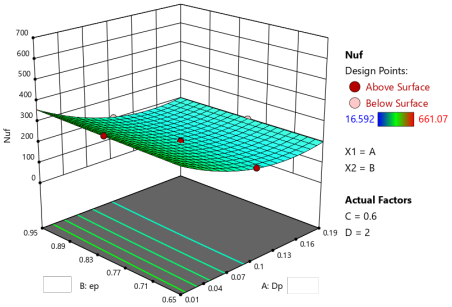

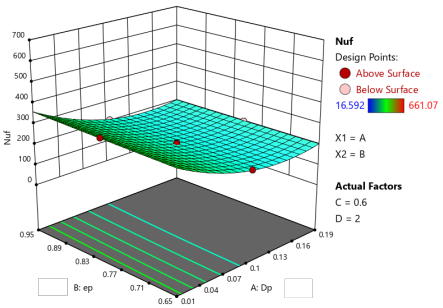

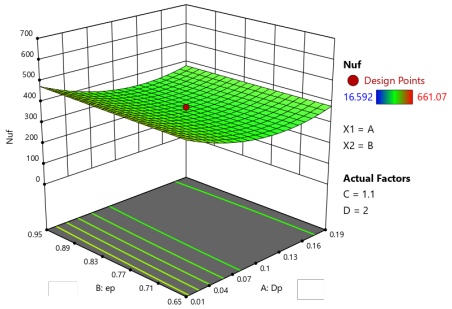

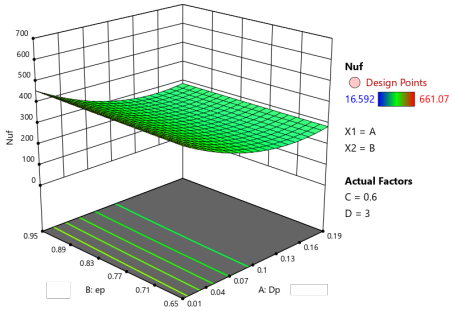

Fig. 4: 3D RS plot of Nuf for Dp vs. ep for different values of wave amplitude $B0$ (1st column) and wave frequency n (2nd column).

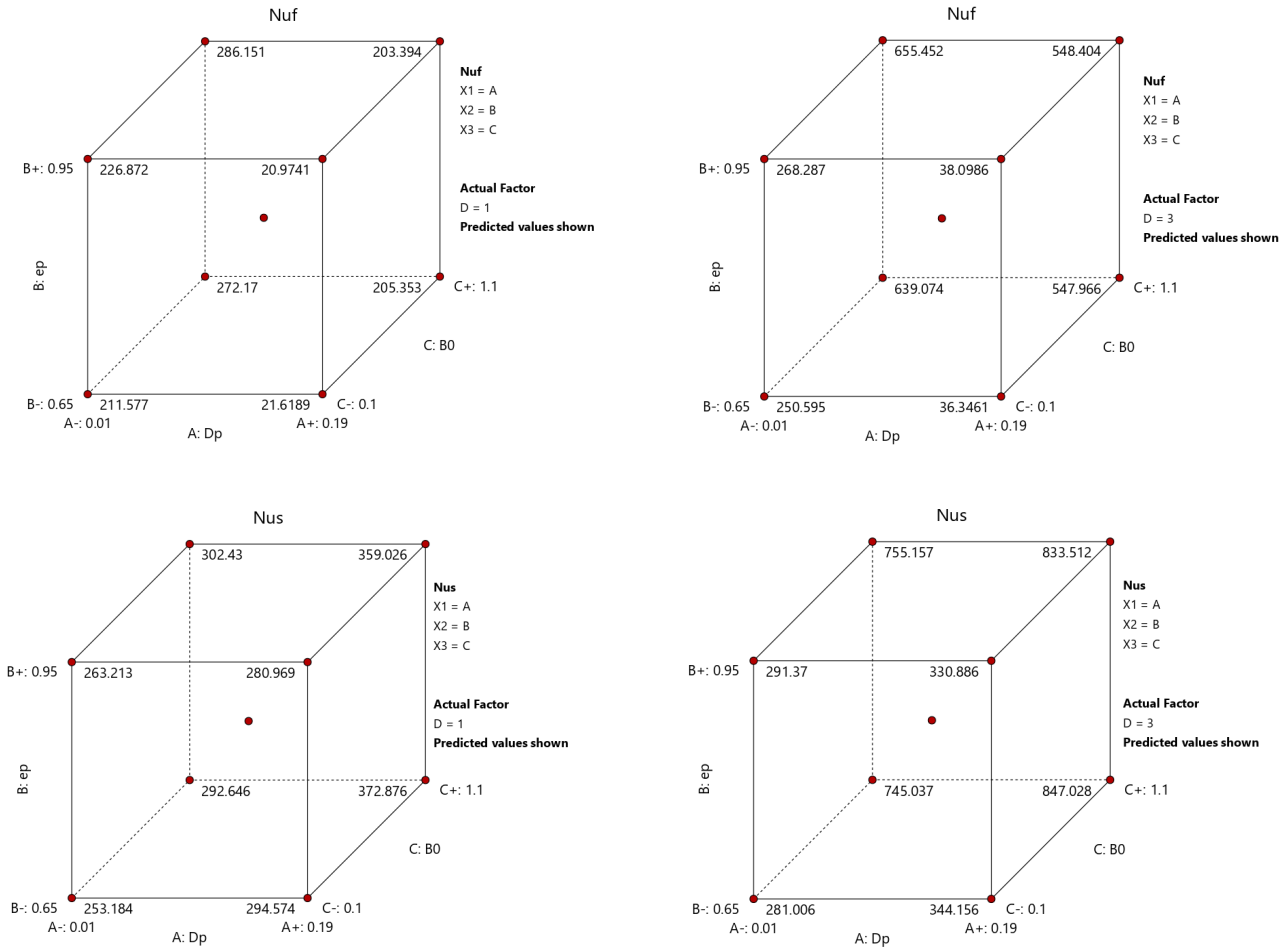

Fig. 5: Cube plot of Nuf (1st row) and Nus (2nd row) for Dp vs. ep vs. $B0$ for different values of the wave frequency $n=1$ (1st column) and $n=3$ (2nd column).

An response surface plot is a graphical representation of the relationship between multiple independent factors (Dp, ep, $B0$, n) and the response variables (Nuf, Nus, and Cf). Figure 4 shows 3D response surface plots that were generated to analyze the impact of (Dp, ep, $B0$, n) on Nuf. Figure 4 illustrates the fascinating interaction of Dp, ep, $B0$, n on the rate of heat transfer in fluid. The value of Nuf increases with the increase of these individual input parameters keeping other parameter values fixed. However, the maximum heat transfer rate occurs when $Dp=0.01$, $ep=0.95$, $B0=1.1$, and $n=3$. Similarly, the minimum heat transfer rate in fluid appears for $Dp=0.19$, $ep=0.95$, $B0=0.1$, and $n=1$ (see, Fig. 5). Besides the maximum and minimum values of Nus are found for $Dp=0.19$, $ep=0.65$, $B0=1.1$, $n=3$ and $Dp=0.01$, $ep=0.65$, $B0=0.1$, $n=1$.

4. Conclusion

Numerical simulations were conducted to investigate the effects of heterogeneous permeability and sinusoidal wall temperature variations on the heat transfer flow inside a rectangular reservoir with a glass bead porous medium. The study aimed to identify the role of various model parameters on the flow and thermal fields. The results showed that the glass bead diameter, porosity, frequency, and wave amplitude significantly affected the heat transfer rate and the friction factor. The optimum heat transfer rate is determined for the studied input parameters.

Acknowledgements

Sultan Qaboos University and IG/SCI/MATH/23/02 and M.S. Alam of Jagannath University, Bangladesh.

References

[1] C. L. Tien and K. Vafai, "Convective and radiative heat transfer in porous media," *Advan. App. Mech.*, vol. *27*, pp. 225-281, 1989.

[2] T. M. Kuzay, "Cryogenic cooling of x-ray crystals using a porous matrix," *Rev. Sci. Instru.*, vol. *63, no.* 1, pp. 468-472, 1992.

[3] D. A. Nield and A. Bejan, Convection in Porous Media. New York, Springer, 2017.

[4] M. Z. Saghir and M. M. Rahman, "Forced convection of Al_2O_3 – Cu, TiO_2 –SiO_2, FWCNT–Fe_3O_4, and ND–Fe_3O_4 hybrid nanofluid in porous media," *Energies*, vol. *13, no.* 11, pp. 2902, 2022.

[5] S. M. Al-Weheibi, M. M. Rahman, M. Z. Saghir and K. Vajravelu, "Three-dimensional free convective heat transmission flow of copper–water nanofluid in a glass bead permeable matrix within a right trapezoidal cavity in consideration of thermal non-equilibrium conditions," *Transp. Porous Media*, vol. *145, no.* 3, pp. 653-681, 2022.

[6] A. R. Al Hajri, I. A. Eltayeb and M. M. Rahman, "Convective instabilities of a Maxwell-Cattaneo porous layer," *J. Porous Media*, *26*(2), 89-114, 2023.

[7] M. S. Astanina and M. A. Sheremet, "Numerical study of natural convection of fluid with temperature-dependent viscosity inside a porous cube under non-uniform heating using local thermal non-equilibrium approach," *Int. J. Thermofluids*, vol. *17*, pp. 100266, 2023.

[8] Y. Varol, F. H. Oztop and I. Pop, "Numerical analysis of natural convection for a porous rectangular enclosure with sinusoidally varying temperature profile on the bottom wall," *Int. Commun. Heat Mass Transfer*, vol. *35, no. 1*, pp. 56-64, 2008.

[9] M. A. Sheremet and F. H. Öztop, "Impact of porous complicated fin and sinusoidal-heated wall on thermogravitational convection of different nanofluids in a square domain," *Int. J. Thermal Sci.*, vol. *168*, pp. 107053, 2021.

[10] A. Amiri and K. Vafai, "Transient analysis of incompressible flow through a packed bed," *Int. J. Heat Mass Transfer*, vol. *41, no.* 24, pp. 4259-4279, 1998

[11] A. Amiri, K. Vafai and T. M. Kuzay, "Effects of boundary conditions on non-Darcian heat transfer through porous media and experimental comparisons," *Numer. Heat Transfer, Part A: Appl.,* vol. *27, no.* 6, pp. 651-664, 1995.

[12] M. M. Rahman, M. Z. Saghir, I. Pop and K. Vajravelu, "Impacts of heterogeneous permeability and sinusoidal wall temperature on the convective heat transmission in a porous medium under local thermal non-equilibrium states," 2024 (submitted for publication).

[13] M. J. Uddin and M. M. Rahman, "Numerical computation of natural convective heat transport within nanofluids filled semi-circular shaped enclosure using nonhomogeneous dynamic model," *Thermal Sci. Eng. Prog.*, vol. *1*, pp. 25-38, 2017.

[14] G. De Vahl Davis, "Natural Convection of air in a square cavity: A Benchmark solution," *Int. J. Numer. Meth. Fluids*, vol. *3*, pp. 249-264, 1983.

[15] G.E.P. Box and K.B. Wilson, "On the experimental attainment of optimum conditions," *J. Royal Stat. Soc.*, vol. 13, no.1, pp. 1-45, 1951.

[16] D. C. Montgomery, Design and Analysis of experiments: Response surface Method and Designs, John Wiley and Sons, Inc, New Jersey, 2005.
[17] N. M. Huda, M. S. Alam and S. M. Chapal Hossain, "Optimization and sensitivity analysis of hydromagnetic convective heat transfer in a square cavity filled with a porous medium saturated by Ag-MgO/water hybrid nanofluid using response surface methodology," *Int. J. Thermofluids*, vol. 22, pp. 100626, 2024.